Materials Reports: Energy 4 (2024) 100271

Contents lists available at ScienceDirect

Materials Reports: Energy

journal homepage: www.keaipublishing.com/en/journals/materials-reports-energy

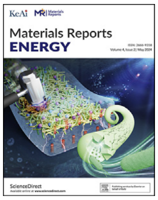

Original Research Report

Unraveling the coordination behavior and transformation mechanism of Cr^{3+} in Fe–Cr redox flow battery electrolytes

Xiaojun Zhao [a], Xinwei Niu [a], Xinyuan Liu [b], Chongchong Wu [c], Xinyu Duan [a], Zhiqi Ma [a,d], Yan Xu [d], Hao Li [e,*], Weijie Yang [b,**]

[a] *Department of Electrical Engineering, North China Electric Power University, Baoding, 071003, PR China*
[b] *Department of Energy Power and Mechanical Engineering, North China Electric Power University, Baoding, 071003, PR China*
[c] *CNOOC Institute of Chemicals & Advanced Materials, Beijing, 102200, PR China*
[d] *Shanghai LongVault Energy Technology Co., Ltd., Shanghai, 201615, PR China*
[e] *Advanced Institute for Materials Research (WPI-AIMR), Tohoku University, Sendai, 980-8577, Japan*

ARTICLE INFO

Keywords:
Fe-Cr redox flow battery
Coordination
Electrolyte
Quantum chemistry computation

ABSTRACT

Currently, the iron chromium redox flow battery (ICRFB) has become a research hotspot in the energy storage field owing to its low cost and easily-scaled-up. However, the activity of electrolyte is still ambiguous due to its complicated solution environment. Herein, we performed a pioneering investigation on the coordination behavior and transformation mechanism of Cr^{3+} in electrolyte and prediction of impurity ions impact through quantum chemistry computations. Based on the structure and symmetry of electrostatic potential distribution, the activity of different Cr^{3+} complex ions is confirmed as $[Cr(H_2O)_5Cl]^{2+} > [Cr(H_2O)_4Cl_2]^{+} > [Cr(H_2O)_6]^{3+}$. The transformation mechanism between $[Cr(H_2O)_6]^{3+}$ and $[Cr(H_2O)_5Cl]^{2+}$ is revealed. We find the metal impurity ions (especially Mg^{2+}) can exacerbate the electrolyte deactivation by reducing the transformation energy barrier from $[Cr(H_2O)_5Cl]^{2+}$ (24.38 kcal mol^{-1}) to $[Cr(H_2O)_6]^{3+}$ (16.23 kcal mol^{-1}). The solvent radial distribution and mean square displacement in different solvent environments are discussed and we conclude that the coordination configuration limits the diffusivity of Cr^{3+}. This work provides new insights into the activity of electrolyte, laying a fundamental sense for the electrolyte in ICRFB.

1. Introduction

Large-scale power storage plays a crucial role in the digestion of new energy and the maintenance of grid stability.[1,2] As a typical large-scale power storage technology, the iron chromium redox flow battery (ICRFB) has returned to the forefront of research.[3–6] The high decoupling of power and capacity achieves its design flexibility.[7] In addition, the abundance of iron and chromium metal materials along with their micro-toxicity make ICRFB a low-cost and high security energy storage solution.[8,9] Since the first iron chromium flow model was proposed by NASA in the 1970s, the ICRFB electrolyte has been ushered into a rapid development stage.[10]

It was found that the Cr^{3+} in negative electrolyte of ICRFB forms complexes like $[Cr(H_2O)_6]^{3+}$, $[Cr(H_2O)_5Cl]^{2+}$, and $[Cr(H_2O)_4Cl_2]^{+}$ with H_2O and Cl^{-} due to solvation effect.[11,12] What's more, further research indicated there are reactivity differences among different complexes, more specifically, the electrode reaction rate constant for $[Cr(H_2O)_6]^{3+}$ is 2.2×10^{-5} cm s^{-1} while that for $[Cr(H_2O)_5Cl]^{2+}$ is 5.6×10^{-3} cm s^{-1}.[13] Moreover, slow transformation exists between them, especially for $[Cr(H_2O)_6]^{3+}$ and $[Cr(H_2O)_5Cl]^{2+}$.[11,12] Thus, their equilibrium plays an important role in the activity of the electrolyte. However, few explorations on microscopic complexes in electrolyte have been reported since 2000. Therefore, to clarify the essence of electrolyte activity, theoretical researches on electrolytes should be carried out urgently, including the

---

* Corresponding author.
** Corresponding author.
E-mail addresses: li.hao.b8@tohoku.ac.jp (H. Li), yangwj@ncepu.edu.cn (W. Yang).

Production and Hosting by Elsevier on behalf of KeAi

https://doi.org/10.1016/j.matre.2024.100271
Received 30 December 2023; Received in revised form 21 February 2024; Accepted 26 February 2024

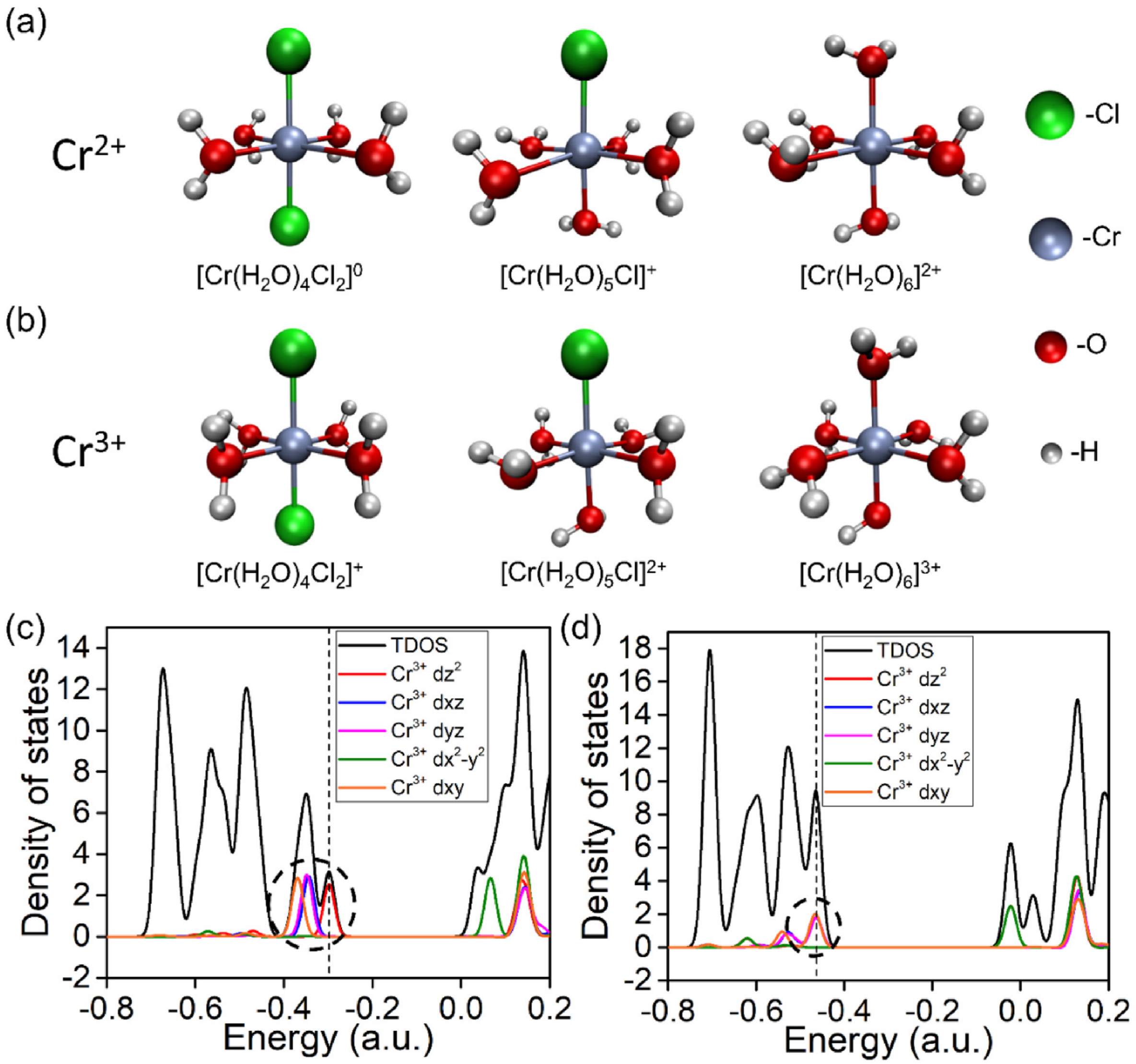

Fig. 1. Complex ion model of Cr^{2+}/Cr^{3+} in ICRFB electrolyte: (a) Cr^{2+}, (b) Cr^{3+}. TDOS and PDOS of *3d* orbital components of Cr^{2+}/Cr^{3+} in CN-6: (c) $Cr(H_2O)_6^{2+}$, (d) $Cr(H_2O)_6^{3+}$. Dotted line corresponds to the HOMO energy level.

Table 1

Geometrical structure parameter and actual charged quantity of Cr^{2+}/Cr^{3+} in complex ion model and reference data in bracket (the actual bond length and bond angle values fluctuate around the values in the table).

Valence	Structure	Cr–O (Å)	Cr–Cl (Å)	O–Cr–O (°)	Cl–Cr–O (°)	AIM Cr
2+	$[Cr(H_2O)_4Cl_2]^0$	2.10, 2.54	2.39		87, 90, 92	1.47
	$[Cr(H_2O)_5Cl]^+$	2.10, 2.48	2.37	84, 87, 88	90, 94, 97	1.52
	$[Cr(H_2O)_6]^{2+}$	2.10, 2.43		89, 91		1.59
3+	$[Cr(H_2O)_4Cl_2]^+$	2.03	2.31		89, 90	1.89
	$[Cr(H_2O)_5Cl]^{2+}$	2.01	2.28	86, 88, 90	91, 94	1.95
	$[Cr(H_2O)_6]^{3+}$	2.00 (1.99)[64]		89, 90, 91		2.01

properties of complex ions and the transformation mechanism between them.

On the other hand, with the rapid development of materials and catalysts, researches of redox flow batteries (RFB) have focused on the preparation of electrodes and catalysts,[14–19] membrane design,[20–22] and additives in the electrolyte. For example, adding NH_4^+ or organic amine to the electrolyte can effectively inhibit the deactivation of Cr^{3+}, so that the electrolyte can maintain good stability and reactivity.[23,24] Introducing indium ions could catalyze the electrochemical reaction of ICRFB and accelerate the reaction kinetics of Cr^{2+}/Cr^{3+}.[25] In addition, to inhibit hydrogen evolution, the neutral electrolytes containing metal chelating agents such as PDTA or EDTA have been successfully applied in ICRFB to replace the acidic electrolytes.[26–30] However, previous researches focused on the influence of artificial additives on the performance of electrolytes, neglecting common impurity ions (Na^+, K^+, Mg^{2+}, etc.) in the electrolyte caused by accompanying minerals of chromium ore and processing purification.[31,32] So far, there has been a lack of literature on the study of common impurity ions in electrolytes of ICRFB, while such systematic and comprehensive study has been conducted on all vanadium flow batteries (VRFB).[33–35] Due to the inevitability of impurity ions in the electrolyte, studying the impact of impurity ions on the electrolyte is highly necessary and can provide a theoretical reference for electrolyte impurity removal.

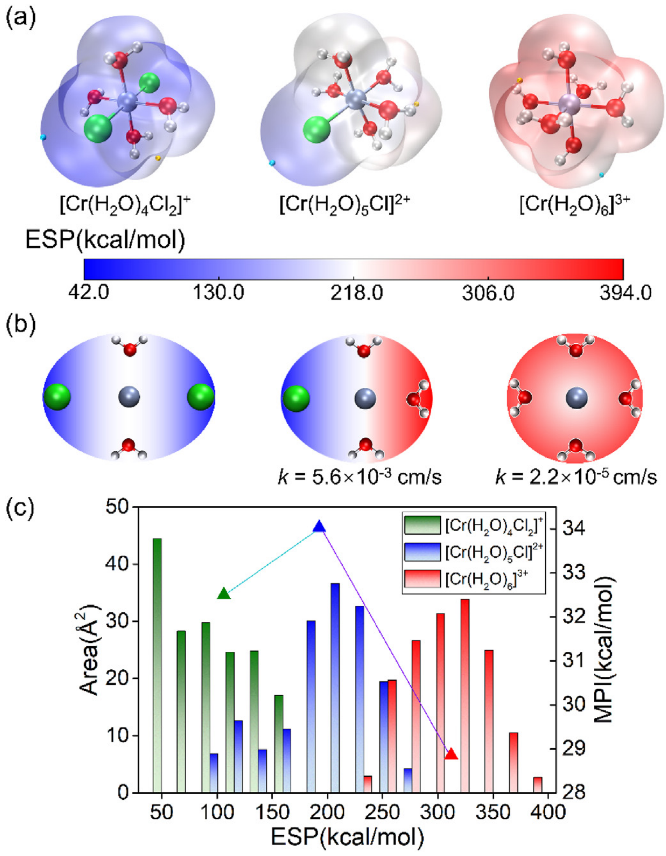

Fig. 2. (a) ESP surface of Cr^{3+} complex ion. The isosurface is 0.001 a.u.; blue dot: ESP_{min}; yellow dot: ESP_{max}. (b) ESP surface schematic of $[Cr(H_2O)_4Cl_2]^+$, $[Cr(H_2O)_5Cl]^{2+}$, $[Cr(H_2O)_6]^{3+}$ respectively. k is the electroreduction reaction rate constant in the experiment.[13] (c) Quantitative ESP distribution of Cr^{3+} complex. Histogram: ESP surface area distribution; line: MPI.

In terms of research methods, previous studies laid particular emphasis on experiments based on material preparation, characterization, and performance testing. Nevertheless, there is a lack of theoretical computations and simulations to profoundly explore the ICRFB electrolyte. Based on the theoretical method, we can reveal molecular behaviors and reaction mechanisms at the micro level, then map to the macroscopic properties, and provide theoretical guidance for material design and performance improvement.[36,37] The successful application of density functional theory (DFT) in other RFBs proves its feasibility.[38–40]

In this work, adopting quantum chemistry computation, the coordination behavior of the Cr^{2+}/Cr^{3+}, the transformation between $[Cr(H_2O)_6]^{3+}$ and $[Cr(H_2O)_5Cl]^{2+}$, and the diffusivity of the electrolyte were studied step by step, taking the prediction of common impurity ions impacts into account. Firstly, the different complex forms of Cr^{2+}/Cr^{3+} were analyzed, and the origin of the difference in electrochemical activity was inferred from the geometric structure and molecule surface electrostatic potential (ESP). Secondly, through the transition state calculation, the transformation mechanism between $[Cr(H_2O)_6]^{3+}$ and $[Cr(H_2O)_5Cl]^{2+}$ was explained by interaction region indicator (IRI) in detail and compared with the situation impurity ions participate. Finally, based on ab initio molecular dynamics (AIMD) simulation, the distribution of solvent molecules in the electrolyte was analyzed by the radial distribution of Cr^{3+}, and the diffusivity of Cr^{3+} in different solvent environments was studied. The objective of this study is to give theoretical insights into the activity of the electrolyte in ICRFB and provide qualitative guidance preliminarily for the preparation of the electrolyte.

2. Methodology

2.1. Quantum chemistry computation details

All the quantum chemistry computations were performed based on the ORCA 5.0.3 package.[41–43] Geometric optimization and frequency analysis were implemented using B3LYP hybrid functional combined with DFT-D3 dispersion correction and def2-TZVP (-f) basis set to guarantee the stability of the optimized structure.[44–46] All structures applied in this paper were local minima on the potential energy surface with no imaginary frequency. The ωB97M−V hybrid functional in conjunction with the def2-TZVP basis set was used to calculate the self-consistent field.[47] Considering the solvation effect of metal ions in aqueous solutions, a hybrid solvent model was adopted during the whole calculation, containing explicit solvent molecules arranged as the first solvation shell and the implicit solvent model (SMD) of water.[48] When searching for the transformation path between $Cr(H_2O)_6^{3+}$ and $Cr(H_2O)_5Cl^{2+}$ and analyzing the impact originating from common impurity ions in the electrolyte, the NEB-TS method was used to ascertain and optimize the transition state (TS) through the initial state (IS) and final state (FS), which was verified successfully by intrinsic reaction coordinate (IRC).[49–51] All the above calculations were accelerated by the RIJCOX.[52]

In order to investigate the diffusivity of the electrolyte, an explicit solvent model of 100 atoms was constructed considering the concentration ratio in the actual electrolyte with the Cr^{3+} as the center. An AIMD simulation of 10 ps with the time-step of 1 fs was carried out under the NVT ensemble,[53] using the B97-3c function and the CSVR thermostat to maintain the temperature.[54] Due to the lack of lattice, the radial distribution function of the system could not be obtained. Therefore, a shell script was compiled to calculate the atomic distance between the central chromium ion and others for obtaining the molecular distribution in the system. ESP and IRI, etc. were all conducted with Multiwfn 3.8 code,[55–59] and the visualization molecular dynamics (VMD) software was used to draw the spatial function image and the statistics of the root mean square displacement (RMSD) in the AIMD results.[60]

2.2. Electrostatic potential

ESP plays an essential role in the discussion of electrostatic interaction.[61] The charge distribution of molecules will generate a corresponding electric potential in the surrounding space. The static distribution generated by the static charge of molecules (including isolated nucleus charge and continuous electron density), i.e., electrostatic potential $V(\mathbf{r})$, can be defined as

$$V(\mathbf{r}) = \sum_{A} \frac{Z_A}{|\mathbf{R}_A - \mathbf{r}|} - \int \frac{\rho(\mathbf{r}')\mathrm{d}\mathbf{r}'}{|\mathbf{r}' - \mathbf{r}|} \tag{1}$$

where Z_A is the nuclear charge of atom A and $\rho(\mathbf{r}')$ is electron density. Through the quantitative analysis of the distribution of electrostatic potential on the surface of molecules, we can obtain the dominant sites of the electrostatic interaction between molecules and also analyze the electrochemical behavior of molecules in the electric field. In a word, electrostatic potential analysis is helpful to study the electrochemical activity of molecules.

2.3. Interaction region indicator

IRI can be used to characterize the interaction between atoms, based on the RDG function.[62] It is a function of electron density $\rho(\mathbf{r})$ and electron density gradient $\nabla\rho(\mathbf{r})$. It can be defined as

$$IRI(\mathbf{r}) = \frac{|\nabla\rho(\mathbf{r})|}{[\rho(\mathbf{r})]^a} \tag{2}$$

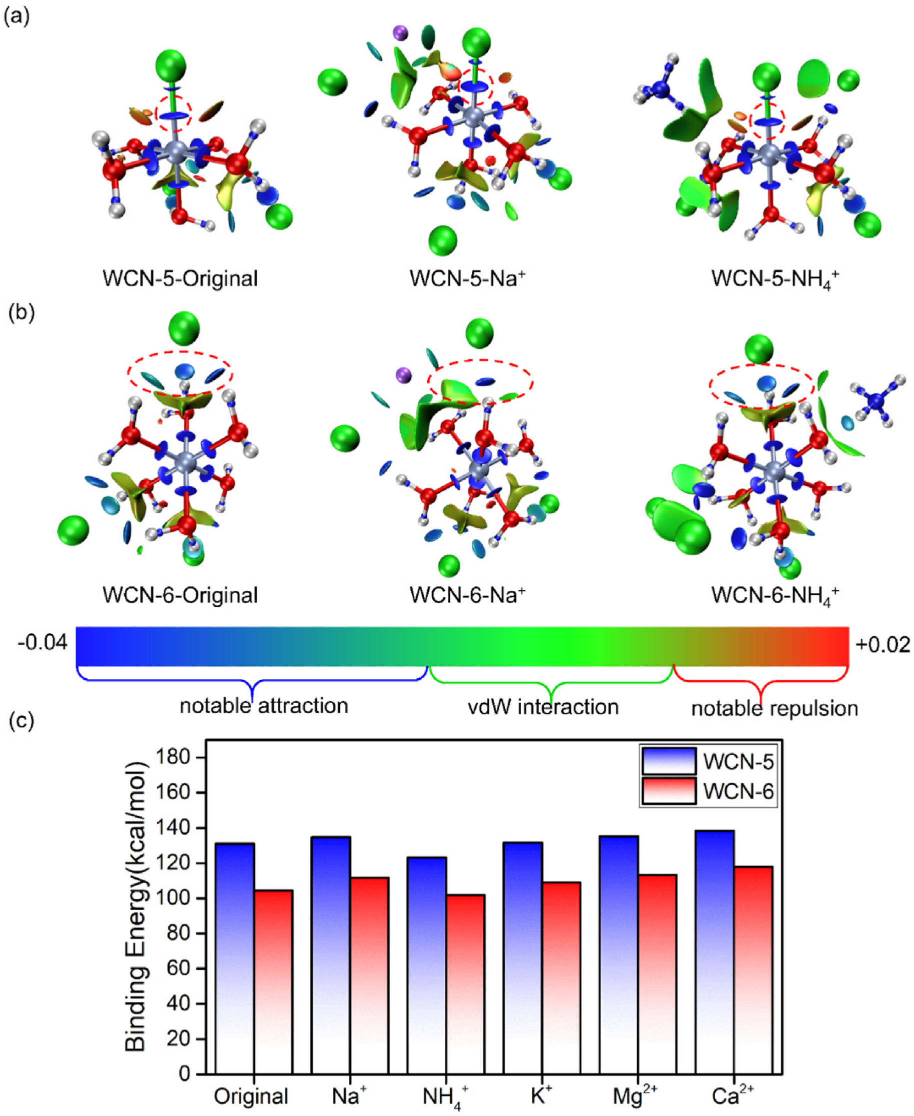

Fig. 3. IRI showing the interaction between Cl^- and WCN-5/WCN-6 in a neutral complex structure: (a) WCN-5-Original, WCN-5-Na^+, WCN-5-NH_4^+; (b) WCN-6-Original, WCN-6-Na^+, CN-6-NH_4^+. Isosurface map of IRI = 1.0 (unit: a.u.). (c) Binding energy of Cl^- in WCN-X-Y (X = 5, 6; Y=Original, Na^+, NH_4^+, K^+, Mg^{2+}, Ca^{2+}).

where $a = 1.1$. IRI analysis has the advantage of visualizing all interactions existing in molecules, whether van der Waals force or chemical bonding. In addition, we can observe the change of interaction intensity between atoms in the reaction process, so as to grasp the core mechanism of the reaction.

2.4. Molecular polarity index

The uneven distribution of molecular charge can be reflected in the distribution of surface electrostatic potential, and the molecular charge distribution determines molecular polarity. Therefore, MPI based on the definition of molecular surface electrostatic potential can measure the molecular polarity.[63] MPI is defined as

$$MPI = (1/A)\iint\limits_S |V(r)|\mathrm{d}S \tag{3}$$

where A is molecular surface area. It can be seen that the meaning of the formula is to integrate the absolute value of the ESP on the whole molecular surface and to calculate the expectation of the area. The existence of a region with very negative or positive ESP indicates that the distribution of molecular charge is uneven, which also illustrates that the molecular polarity is large, and the molecular polarity index will be large.

However, the definition of MPI is only applicable to neutral molecules. For a charged system, the absolute value of ESP in the formula loses its meaning because the whole molecule presents positive or negative electricity. Especially when comparing the polarity between molecules with different charges, the MPI of the molecules with high charges must be greater than that of the molecules with low charges, but it cannot reflect the uneven distribution of ESP. Therefore, in order to make MPI applicable to charged systems, the definition of MPI can be corrected with the average of ESP $\overline{V}$ (r) as follows

$$MPI = (1/A)\iint\limits_S |V(r) - \overline{V}(r)|\mathrm{d}S \tag{4}$$

By introducing $\overline{V}$ (r) into the definition, the ESP distribution of the charged system is pulled to the neutral reference, guaranteeing the applicability of MPI. The MPI of the neutral molecule $[Cr(H_2O)_4Cl_2]^0$ calculated by formula (3) and formula (4) in Table S1 are 30.29 kcal mol^{-1} and 30.31 kcal mol^{-1} respectively. Table S2 shows more neutral species, and we can see this definition is also applicable to the neutral system.

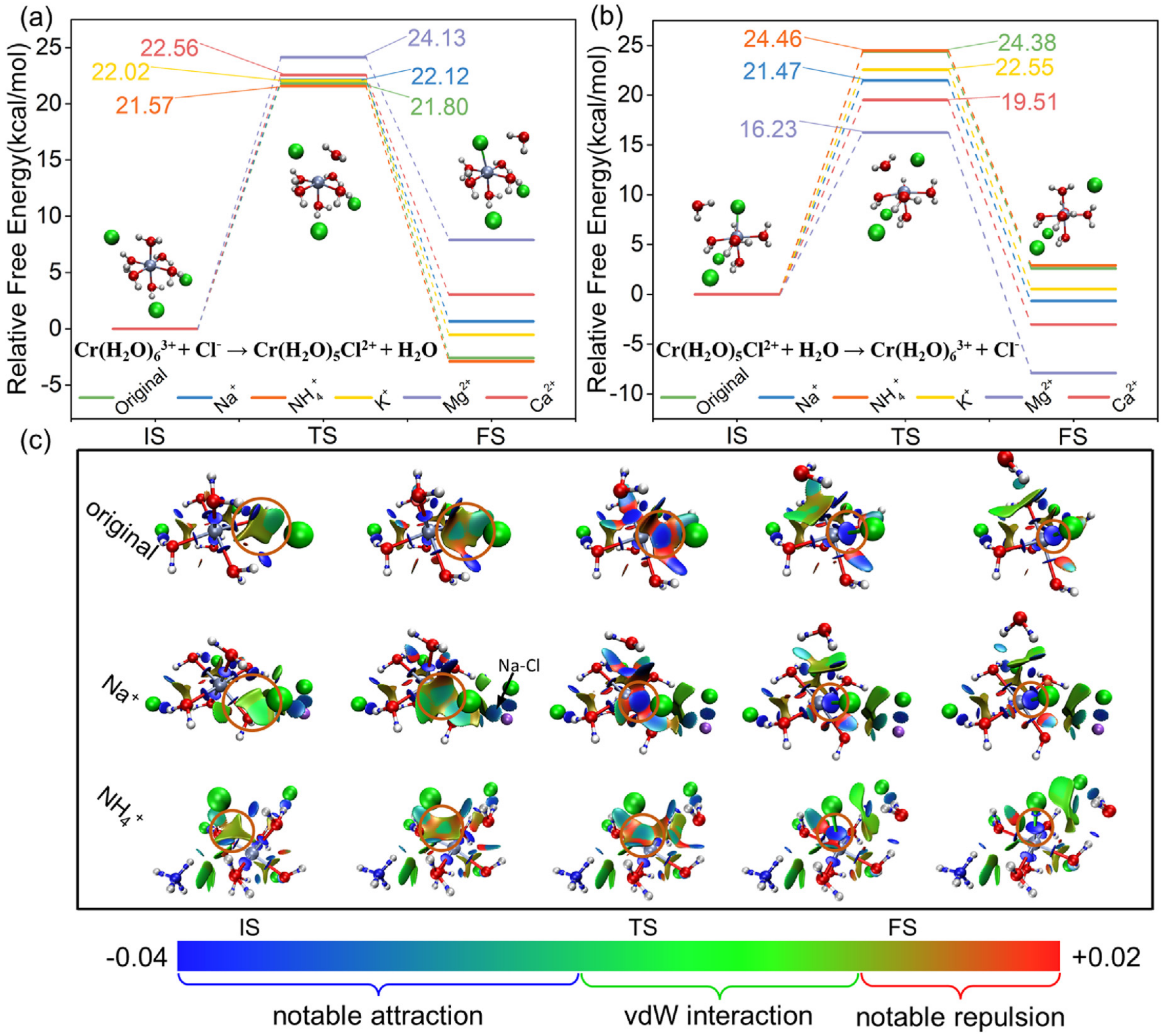

Fig. 4. Relative free energy and IRI images of complex ion transformation: (a) WCN-6 to WCN-5, (b) WCN-5 to WCN-6. (c) IRI change of WCN-6 to WCN-5 selected Original, Na^+ and NH_4^+. The interaction in a brown circle in the key interaction of Cl^-. Isosurface map of IRI = 1.0 (unit: a.u.).

3. Result and discussion

3.1. Cr complex ion in the electrolyte

3.1.1. Structure characteristics of Cr^{2+}/Cr^{3+} complex ion

Three complexation forms of Cr^{3+}, including $[Cr(H_2O)_4Cl_2]^+$, $[Cr(H_2O)_5Cl]^{2+}$ and $[Cr(H_2O)_6]^{3+}$ were studied. Fig. 1a and b shows the optimized coordinate structure of Cr^{2+}/Cr^{3+}. It is depicted that the Cr^{2+}/Cr^{3+} forms an octahedral coordination structure with six ligands in the solvent environment, which is also confirmed in the experiment.[64] However, from the difference in structural parameters such as bond length and bond angle shown in Table 1, the octahedral configurations of $[Cr(H_2O)_5Cl]^{2+}$ and $[Cr(H_2O)_4Cl_2]^+$ exhibit structural distortion partly. As the Cr–Cl is larger than Cr–O and the repulsion of single Cl^- on equator H_2O ligands in $[Cr(H_2O)_5Cl]^{2+}$, the structural symmetry follows the order of $[Cr(H_2O)_6]^{3+} > [Cr(H_2O)_4Cl_2]^+ > [Cr(H_2O)_5Cl]^{2+}$. The structural symmetry can reflect complex ion activity to a certain extent. For example, it is difficult for the H_2O ligand to detach from the complex ion due to the consistent strength of the Cr–O coordination bond in $[Cr(H_2O)_6]^{3+}$. As for $[Cr(H_2O)_5Cl]^{2+}$, the introduction of Cl^- leads to structural distortion of the complex, making it easier for the ligand to detach.[65] Therefore, $[Cr(H_2O)_5Cl]^{2+}$ is more easily to be adsorbed onto the electrode and undergoes electroreduction. Interestingly, we find a significant difference in Cr–O length (2.10 Å and 2.43 Å) in $[Cr(H_2O)_6]^{3+}$ of Cr^{2+} as Table 1 shows. We can compare the PDOS of Cr^{2+}/Cr^{3+} in Fig. 1c and d for further analysis. In Cr^{2+}, except for d_{x2-y2}, the others are staggered near the HOMO level. The uneven distribution leads to the bonding anisotropy of Cr^{2+}. Conversely, the consistent distribution of d_{xy}, d_{yz} and d_{xz} in Cr^{3+} indicates the isotropy of bonding.

3.1.2. Electrostatic potential distribution of Cr^{3+} complex ion

To further account for the activity differences of three Cr^{3+} complex ions, the surface ESP distribution was plotted and analyzed quantitatively in Fig. 2a (Cr^{2+} in Fig. S1). Firstly, due to different charge amounts, the ESP distribution region of three complex ions is relatively dispersed. Furthermore, the low ESP mainly occurs in the corresponding region of Cl^-, while the high region corresponds to the H mostly. According to this rule, the ESP of the surface presents a uniform distribution in $[Cr(H_2O)_6]^{3+}$. In $[Cr(H_2O)_4Cl_2]^+$, although the existing low ESP region corresponds to Cl^-, its structure still has a certain symmetry. For the $[Cr(H_2O)_5Cl]^{2+}$ structure, due to its structural asymmetry and the single Cl^-, the distribution of its ESP is relatively distinct, the maximum and minimum ESP points of $[Cr(H_2O)_5Cl]^{2+}$ structure are distributed on the opposite sides. Owing to the special ESP distribution structure, $[Cr(H_2O)_5Cl]^{2+}$ structure has the strongest polarity. Fig. 2b vividly shows the ESP distribution characteristics of three complex ions. In the electric field provided by the electrodes, the electric orientation of $[Cr(H_2O)_5Cl]^{2+}$ complex ion is more distinct as the effect of orientation

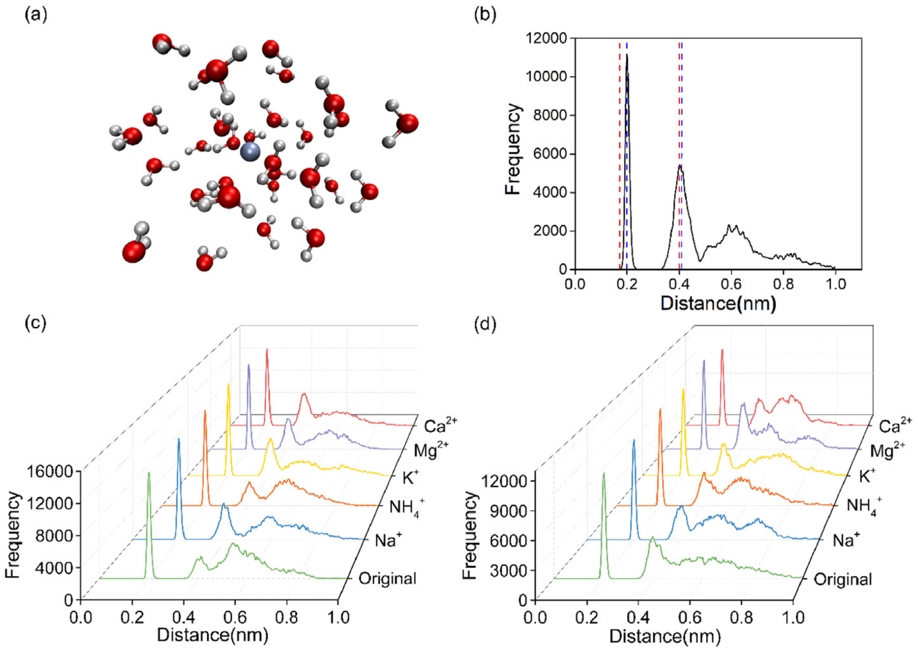

Fig. 5. (a) Model of Cr^{3+} in pure water. (b) H_2O radial distribution centered on Cr^{3+}. Radial distribution of H_2O centered on Cr^{3+} in (c) WCN-5 and (d) WCN-6. Note: the dashed lines in (b) indicate the characteristic peaks calculated by different methods in previous literature. Red: AIMD. Blue: PBE_0.[68,69]

polarization, thereby improving the electric double layer.[66] Under the effect of the electric field force difference from its poles, the $[Cr(H_2O)_5Cl]^{2+}$ is easier to lose ligand from the coordination structure and be adsorbed to the electrode surface, providing convenience for the occurrence of inner sphere reaction.[67]

To measure the molecular polarity of complex ions quantitatively, Fig. 2c shows the quantitative ESP distribution. The wildest distribution is the $[Cr(H_2O)_5Cl]^{2+}$, with a range from 102.05 kcal mol^{-1} to 282.79 kcal mol^{-1} for Cr^{3+}. Based on the ESP, the molecular polarity index (MPI) used for analysis and comparison is also shown in Fig. 2c. It displays that the order of MPI is $[Cr(H_2O)_5Cl]^{2+} > [Cr(H_2O)_4Cl_2]^{+} > [Cr(H_2O)_6]^{3+}$ for Cr^{3+}, which is basically consistent with the previous ESP analysis. The electroreduction rate constant obtained through experiments can also verify the above conclusion.[13] Overall, the above analysis verifies the activity difference of complex ions and clarifies the affecting factor from the symmetry of ESP distribution.

3.2. *Transformation mechanism between $[Cr(H_2O)_5Cl]^{2+}$ and $[Cr(H_2O)_6]^{3+}$*

Due to the activity of complex ions $[Cr(H_2O)_5Cl]^{2+} > [Cr(H_2O)_4Cl_2]^{+} > [Cr(H_2O)_6]^{3+}$, it is of great necessity to reveal the transformation mechanism between two of them for increasing the proportion of $[Cr(H_2O)_5Cl]^{2+}$ in the electrolyte. As the amount of $[Cr(H_2O)_4Cl_2]^{+}$ in electrolyte is much smaller during charge/discharge compared with $[Cr(H_2O)_5Cl]^{2+}$ and $[Cr(H_2O)_6]^{3+}$, therefore, more focus should be paid to investigate the transformation between $[Cr(H_2O)_5Cl]^{2+}$ and $[Cr(H_2O)_6]^{3+}$, as shown in the following reaction.

$$\left[Cr(H_2O)_6\right]^{3+} + Cl^- \leftrightarrow \left[Cr(H_2O)_5Cl\right]^{2+} + H_2O \qquad (5)$$

To avoid interference from charged ions with different valence states, chloride ions are added to ensure the electrical neutrality of the system as $[Cr(H_2O)_6]Cl_3$ and $[Cr(H_2O)_5Cl]Cl_2$. Based on the number of water molecules in the first coordination layer, the complex ions are defined as WCN-6 and WCH-5 respectively. In addition, considering the possible coexistence of impurity ions in the reagent used for preparing electrolytes, the comparison of the original model and adding-impurity model (Original, Na^+, NH_4^+, K^+, Mg^{2+}, Ca^{2+}) also needs detailed exploration.

3.2.1. *Interaction between Cl^- and complex ions*

Before the transformation, the interaction of Cl^- with WCN-5 and WCN-6 was studied (as shown in Fig. 3). Other IRI can be seen in Fig. S2. The binding energy of Cl^- with WCN-5 is generally greater than that with WCN-6 (Fig. 3c). We can analyze the interaction strength through IRI. Fig. 3a shows that Cl^- forms a strong coordinate bond with the central Cr^{3+} in WCN-5. While in WCN-6, Cl^- only combines with H in H_2O ligands, leading to a smaller binding energy of WCN-6 compared with WCN-5. In addition, the introduction of impurity metal ions can slightly increase the binding energy due to the interaction between impurity metal ions and Cl^-. However, NH_4^+ has the opposite effect. The interaction between Cl^- and complex ions provides a reference for the energy barrier changes during the subsequent transformation process.

3.2.2. *Transformation mechanism between $Cr(H_2O)_5Cl^{2+}$ and $Cr(H_2O)_6^{3+}$*

Fig. 4 shows the transformation between WCN-6 and WCN-5 while the interaction change was analyzed using IRI. Fig. 4a shows the transformation energy barrier of WCN-6 to WCN-5, except NH_4^+, the introduction of impurity ions leads to an increase of energy barrier as $Mg^{2+} > Ca^{2+} > Na^+ > K^+ >$ Original $> NH_4^+$, indicating that the metal impurity ions will hinder the transformation of WCN-6 to active WCN-5, whereas NH_4^+ can promote it slightly. As for the opposite process shown in Fig. 4b, the energy barrier follows the order of $NH_4^+ >$ Original $> K^+ > Na^+ > Ca^{2+} > Mg^{2+}$, which illustrates that metal impurity ions will promote the transformation of active WCN-5 to WCN-6. Especially, Mg^{2+} outstands from these metal impurity ions with a transformation energy barrier decreasing from 24.38 kcal mol^{-1} to 16.23 kcal mol^{-1}. Therefore, metal impurity ions will boost the deactivation of electrolyte. On the contrary, it is noted that NH_4^+ results in a small increase in the energy barrier, inhibiting the transformation to inactive WCN-6. Therefore, NH_4^+ plays a positive role in preventing the inactivation of the electrolyte, which fits the experimental result described in previous literature.[23]

In Fig. 4c, the essence of this transformation is that Cl^- occupies the coordination site of H_2O. During the transformation process, Cl^- is repelled by surrounding water molecules, corresponding to the energy barrier. When metal impurity ions were introduced, taking Na^+ as an example, there was a strong electrostatic attraction between Cl^- and Na^+. This indicates that Cl^- bears greater resistance in the transformation,

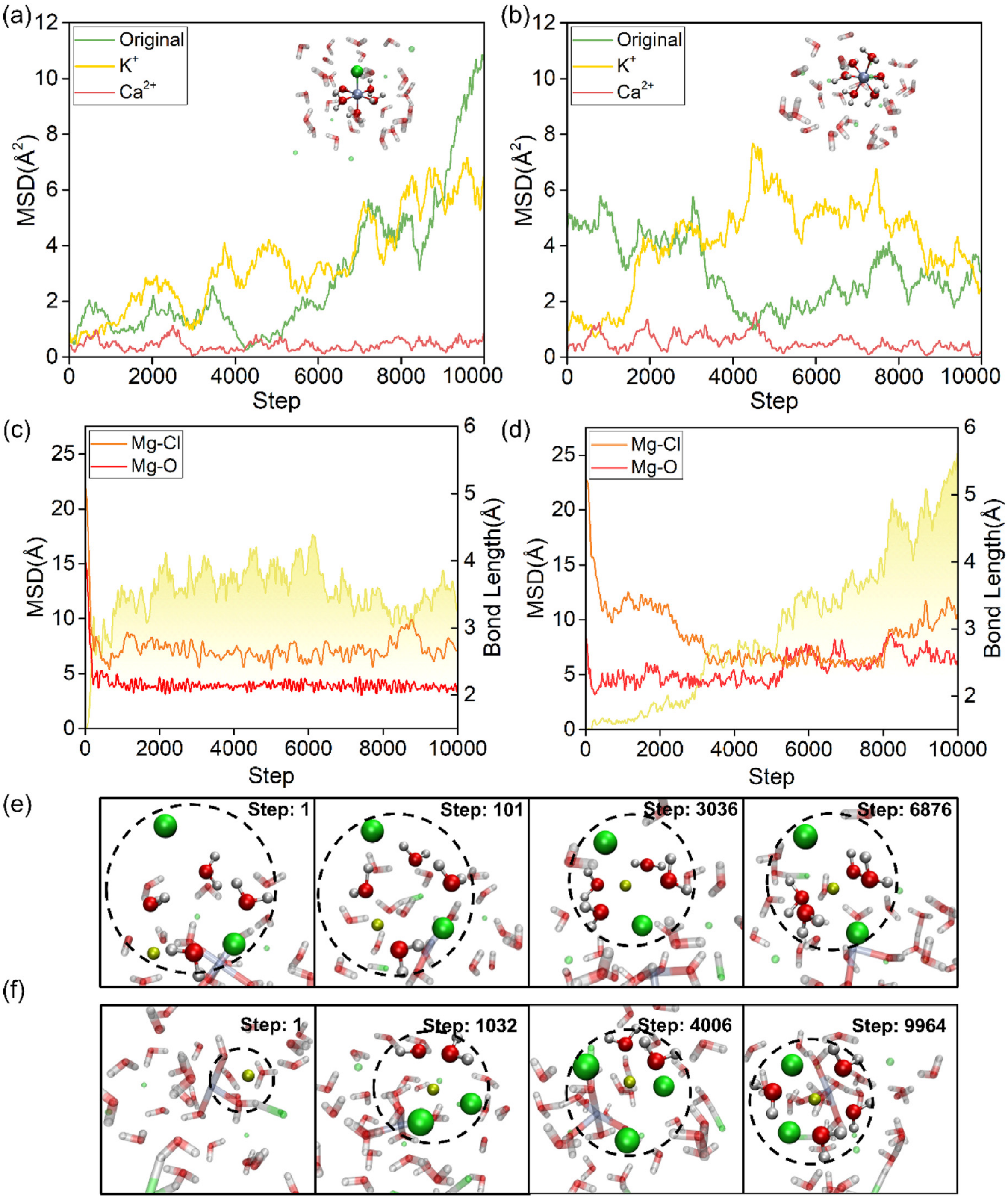

Fig. 6. Selected MSDs of Cr^{3+} in each electrolyte model: (a) WCN-5-Original, WCN-5-K^+, WCN-5-Ca^{2+}, (b) WCN-6-Original, WCN-6-K^+, WCN-6-Ca^{2+}. The line graphs are the average bond length changes of Mg–O and Mg–Cl and the area graphed are the MSD of Mg^{2+}: (c) WCN-5, (d) WCN-6. The configuration of Mg^{2+} and peripheral solvent molecules during AIMD simulation: (e) WCN-5, (f) WCN-6.

leading to an increase in the energy barrier. Interestingly, we observe that it is difficult for NH_4^+ to interact with Cl^-. Therefore, NH_4^+ has little influence on the transformation process. Similarly, we can also analyze the reverse process of transformation (WCN-5 to WCN-6). In conclusion, from the perspective of mutual transformation between active WCN-5 and inactive WCN-6, metal impurity ions will give rise to the inactivation of the electrolyte while NH_4^+ has a slight positive effect on the stable existence of active ions. This provides a qualitative reference for impurity removal from the electrolyte.

3.3. Dynamic migration trajectory of Cr^{3+}

To investigate the dynamic properties and solvent distribution of the electrolyte, the AIMD simulation was carried out based on the electrolyte model (Fig. S7) built according to the actual concentration ratio, while qualitatively considering the influence of impurity ions. The electrolyte model could remain basically stable during the simulation (Fig. S8).

3.3.1. *Coordination characteristics of Cr^{3+} in different solvent environments*

Fig. 5b displays the H_2O distribution law in the Cr^{3+}-pure water model (Fig. 5a): the Cr–O distance reaches the first peak near 0.2 nm, corresponding to the first solvation shell of Cr^{3+}. Then, a vacuum layer appears from 0.26 nm to 0.33 nm. The second characteristic peak appears near 0.4 nm. The peak distribution of the Cr–O distance is consistent with previous literature.[68,69] With the increase of distance, H_2O tends to be more uniform. The obtained distribution law of H_2O near Cr^{3+} can provide a reference for the distribution of electrolyte containing impurity ions in ICRFB.

Fig. 5c and d shows the H_2O distribution of the solvation model built around the WCN-5 and WCN-6 of Cr^{3+}, respectively. It can be seen that the Cl^- and impurity ions mainly affect the second characteristic peak and the area after it. The first solvent shell remains stable throughout the simulation as Fig. S6 shows. The first characteristic peak ratio of the two is approximately 6:5, matched with the coordination structure. In addition, the second characteristic peaks of WCN-6-Original and WCN-6-NH_4^+ are distorted, but the addition of metal ions can avoid such distortion. The specific difference in solvent molecular distribution can be explained from the perspective of the joint influence of Cr^{3+} and the impurity ion solvation effect.

3.3.2. *Diffusivity rate of Cr^{3+} in different solvent environments*

As Fig. 6a shows the Cr^{3+} in the WCN-5-Original has the most excellent diffusivity compared with other models. When impurity ions exist, a significant decrease in diffusivity is detected. However, as presented in Fig. 6b, the Cr^{3+} in the WCN-6 does not satisfy the Stokes-Einstein relation, showing the fluctuation of molecular motion. By comparing the two models, it is apparent that the first solvent shell distribution of Cr^{3+} has a greater impact on its diffusivity. From the aspect of coordination structure, the symmetrical solvation shell restricts the diffusion of Cr^{3+} in WCN-6, which is manifested by oscillations at the reference site. In contrast, the weak symmetry of the WCN-5 leads to the directivity of Cr^{3+} diffusion, which encounters less hindrance in the diffusion process. From the aspect of impurity ions, the impurity ions will also form a solvation shell in the electrolyte, and limit the diffusion of Cr^{3+} through it. The excellent diffusivity of Cr^{3+} in the WCN-5-Original provides convenience for the rapid migration in the electrolyte, which plays an essential role in electrolyte activity.

Interestingly, when studying the diffusion of impurity ions, the phenomena found can verify the above analysis. Fig. S9 shows the MSD curve of impurity ions. It can be found that the MSD of other systems, except WCN-5-Mg^{2+}, exhibit a positive correlation with time, consistent with the Stokes-Einstein relationship. For this purpose, WCN-5-Mg^{2+} and WCN-6-Mg^{2+} were compared in detail. In Fig. 6c, from the average length of Mg–O and Mg–Cl, it can be seen that the solvent shell is very stable, greatly limiting the diffusion of Mg^{2+}. Moreover, after rapid migration, Mg^{2+} is surrounded by a symmetric solvent shell (similar to $[Cr(H_2O)_4Cl_2]^+$) formed by two Cl^- and four H_2O, then no diffusion (Fig. 6e). In contrast, the length of Mg–O and Mg–Cl shows significant fluctuations (Fig. 6d), and there is no fixed solvent distribution around Mg^{2+} (Fig. 6f), which makes the diffusion of Mg^{2+} freer. As can be seen from Fig. S10, the WCN-5-Mg^{2+} and WCN-6-Mg^{2+} have different solvent distribution characteristics. Similar conclusions about the diffusivity of ions and their local chemical environment were also obtained in solid electrolytes.[70–72] Additionally, it proves that the first solvent shell has a significant impact on diffusion performance; on the other hand, it illustrates that the solvation effect of impurity ions will interfere with the distribution of solvent in the electrolyte, thus affecting the diffusion of Cr^{3+}.

In addition, it is interesting to note that K^+ is special. In WCN-5 structures with impurity ions, the WCN-5-K^+ model has the best diffusivity and can well reflect the diffusion law. In WCN-6 structures containing impurity ions, K^+ makes the diffusion of Cr^{3+} more active. To sum up, from the perspective of solvent shell configuration and impurity ions solvation, it is concluded that the diffusivity of WCN-5-Original is better than that of WCN-6-Original and most impurity ions will limit the diffusion of Cr^{3+}. Therefore, increasing the proportion of the WCN-5 complex ion in the electrolyte is the principal goal. Considering the coexistence of WCN-5 and WCN-6 in the actual electrolyte, it is appropriate to release restrictions on the K^+ removal.

4. Conclusion

In summary, to explore the coordination behavior and transformation mechanism of Cr^{3+} in ICRFB electrolyte, we investigate the ESP, transformation barrier, and ion diffusion characteristics of chromium complex ion in the electrolyte. The symmetry of electrostatic potential distribution is the origin of the activity of Cr^{3+} complex ions in the electrolyte. The sequence of activity for different Cr^{3+} complex ions is $[Cr(H_2O)_5Cl]^{2+} > [Cr(H_2O)_4Cl_2]^+ > [Cr(H_2O)_6]^{3+}$, corresponding with the current experimental results. Except for NH_4^+, other metal impurity ions will increase the transformation barrier from inactive WCN-6 to active WCN-5 and reduce the reverse through the strong electrostatic attraction with Cl^-, especially for Mg^{2+}. We predict that metal impurity ions have a significantly negative influence on transformation, which results in electrolyte inactivation. Finally, through MSD, we draw a conclusion that the Cr^{3+} diffusivity in the WCN-5-Original model is the best, and the conclusion is figured out through the radial solvent distribution and impurity ion solvation. We can also draw inspiration from the above conclusions. First, to improve the activity of Cr^{3+} complexes, the proportion of active WCN-5 in the electrolyte should be increased as much as possible by introducing proper additives such as NH_4Cl. In addition, to suppress the deactivation of the electrolyte, qualitative suggestions are proposed preliminarily for impurity removal from the electrolyte: Mg^{2+}, Ca^{2+} and Na^+ must be removed, and the requirement for K^+ can be relaxed.

Declaration of competing interest

The authors declare the following financial interests/personal relationships which may be considered as potential competing interests: Chongchong Wu is currently employed by CNOOC Institute of Chemicals & Advanced Materials; Zhiqi Ma and Yan Xu are currently employed by Shanghai LongVault Energy Technology Co., Ltd. The research project is funded by Beijing PARATERA Tech Co., Ltd.

Acknowledgments

This work was supported by the Fundamental Research Funds for the Central Universities (2023MS125). The authors acknowledge Beijing PARATERA Tech Co., Ltd. for providing computational resources.

Appendix A. Supplementary data

Supplementary data to this article can be found online at https://doi.org/10.1016/j.matre.2024.100271.

References

1. Vanýsek P, Novák V. Redox flow batteries as the means for energy storage. *J Energy Storage*. 2017;13:435–441.
2. Hunter CA, Penev MM, Reznicek EP, Eichman J, Rustagi N, Baldwin SF. Techno-economic analysis of long-duration energy storage and flexible power generation technologies to support high-variable renewable energy grids. *Joule*. 2021;5:2077–2101.
3. Emmett RK, Roberts ME. Recent developments in alternative aqueous redox flow batteries for grid-scale energy storage. *J Power Sources*. 2021;506:230087.
4. Yang Z, Zhang J, Kintner-Meyer MC, et al. Electrochemical energy storage for green grid. *Chem Rev*. 2011;111:3577–3613.
5. Wang W, Luo Q, Li B, Wei X, Li L, Yang Z. Recent progress in redox flow battery research and development. *Adv Funct Mater*. 2013;23:970–986.
6. Sun C, Zhang H. Review of the development of first-generation redox flow batteries: iron-chromium system. *ChemSusChem*. 2022;15:e202101798.

7. Noack J, Roznyatovskaya N, Herr T, Fischer P. The chemistry of redox-flow batteries. *Angew Chem Int Ed*. 2015;54:9776–9809.
8. Zeng YK, Zhao TS, An L, Zhou XL, Wei L. A comparative study of all-vanadium and iron-chromium redox flow batteries for large-scale energy storage. *J Power Sources*. 2015;300:438–443.
9. Li B, Liu J. Progress and directions in low-cost redox-flow batteries for large-scale energy storage. *Natl Sci Rev*. 2017;4:91–105.
10. Thaller LH. Electrically rechargeable redox flow cells. In: *9th Intersociety Energy Conversion Engineering Conference*. 9th Intersociety energy conversion engineering conference; 1974:924–928.
11. Gates HS, King EL. A study of the equilibria in acidic chromium (III) chloride solutions$^{1\text{-}3}$. *J Am Chem Soc*. 1958;80:5011–5015.
12. Johnson DA, Reid MA. Chemical and electrochemical behavior of the Cr (III)/Cr (II) half-cell in the iron-chromium redox energy storage system. *J Electrochem Soc*. 1985; 132:1058–1062.
13. Weaver MJ, Anson FC. Distinguishing between inner-and outer-sphere electrode reactions. Reactivity patterns for some chromium (III)-chromium (II) electron-transfer reactions at mercury electrodes. *Inorg Chem*. 1976;15:1871–1881.
14. Park M, Ryu J, Wang W, Cho J. Material design and engineering of next-generation flow-battery technologies. *Nat Rev Mater*. 2016;2:1–18.
15. Ahn Y, Moon J, Park SE, Shin J, Choi JW, Kim KJ. High-performance bifunctional electrocatalyst for iron-chromium redox flow batteries. *Chem Eng J*. 2021;421: 127855.
16. Cheng D, Tian M, Wang B, et al. One-step activation of high-graphitization N-doped porous biomass carbon as advanced catalyst for vanadium redox flow battery. *J Colloid Interface Sci*. 2020;572:216–226.
17. He X, Li L, Yan S, et al. Advanced electrode enabled by lignin-derived carbon for high-performance vanadium redox flow battery. *J Colloid Interface Sci*. 2024;653: 1455–1463.
18. Zhang H, Tan Y, Li J, Xue B. Studies on properties of rayon-and polyacrylonitrile-based graphite felt electrodes affecting Fe/Cr redox flow battery performance. *Electrochim Acta*. 2017;248:603–613.
19. Ma Y, Qaisrani NA, Ma L, et al. Side chain hydrolysis method to prepare nanoporous membranes for vanadium flow battery application. *J Membr Sci*. 2018;560:67–76.
20. Peng S, Wu X, Yan X, et al. Polybenzimidazole membranes with nanophase-separated structure induced by non-ionic hydrophilic side chains for vanadium flow batteries. *J Mater Chem A*. 2018;6:3895–3905.
21. Li F, Duan G, Wang Z, et al. Highly efficient recovery of hydrogen from dilute H_2-streams using $BaCe_{0.7}Zr_{0.1}Y_{0.2}O_{3\text{-}\delta}$/Ni-$BaCe_{0.7}Zr_{0.1}Y_{0.2}O_{3\text{-}\delta}$ dual-layer hollow fiber membrane. *Sep Purif Technol*. 2022;287:120602.
22. Wang M, Wang Z, Tan X, Liu S. Externally self-supported metallic nickel hollow fiber membranes for hydrogen separation. *J Membr Sci*. 2022;653:120513.
23. Zhang L, Zhang W. Improvements over the deactivation of the Cr^{3+}/Cr^{2+} redox couple with N-alkylamines and NH_4Cl additives. *Chin J Power Sources*. 1991;2:26–28.
24. Cheng DS, Reiner A, Hollax E. Activation of hydrochloric acid-$CrCl_3{\cdot}6H_2$ solutions with N-alkyfamines. *J Appl Electrochem*. 1985;15:63–70.
25. Wang S, Xu Z, Wu X, et al. Excellent stability and electrochemical performance of the electrolyte with indium ion for iron–chromium flow battery. *Electrochim Acta*. 2021; 368:137524.
26. Bae CH, Roberts EPL, Dryfe RAW. Chromium redox couples for application to redox flow batteries. *Electrochim Acta*. 2002;48:279–287.
27. Bamgbopa MO, Shao-Horn Y, Almheiri S. The potential of non-aqueous redox flow batteries as fast-charging capable energy storage solutions: demonstration with an iron–chromium acetylacetonate chemistry. *J Mater Chem A*. 2017;5:13457–13468.
28. Singh V, Kim S, Kang J, Byon HR. Aqueous organic redox flow batteries. *Nano Res*. 2019;12:1988–2001.
29. Waters SE, Robb BH, Marshak MP. Effect of chelation on iron-chromium redox flow batteries. *ACS Energy Lett*. 2020;5:1758–1762.
30. Robb BH, Farrell JM, Marshak MP. Chelated chromium electrolyte enabling high-voltage aqueous flow batteries. *Joule*. 2019;3:2503–2512.
31. Murthy YR, Tripathy SK, Kumar CR. Chrome ore beneficiation challenges & opportunities–A review. *Miner Eng*. 2011;24:375–380.
32. Zhang J, Xie W, Chu S, et al. Sufficient extraction of Cr from chromium ore processing residue (COPR) by selective Mg removal. *J Hazard Mater*. 2022;440: 129754.
33. Cao L, Skyllas-Kazacos M, Menictas C, Noack J. A review of electrolyte additives and impurities in vanadium redox flow batteries. *J Energy Chem*. 2018;27:1269–1291.
34. Pahlevaninezhad M, Pahlevani M, Roberts EP. Effects of aluminum, iron, and manganese sulfate impurities on the vanadium redox flow battery. *J Power Sources*. 2022;529:231271.
35. Park JH, Park JJ, Lee HJ, Min BS, Yang JH. Influence of metal impurities or additives in the electrolyte of a vanadium redox flow battery. *J Electrochem Soc*. 2018;165: A1263.
36. Burnea FKB, Shi H, Ko KC, Lee JY. Reduction potential tuning of first row transition metal MIII/MII (M= Cr, Mn, Fe, Co, Ni) hexadentate complexes for viable aqueous redox flow battery catholytes: a DFT study. *Electrochim Acta*. 2017;246:156–164.
37. Ng MF, Zheng J, Wu P. Evaluation of Sn nanowire encapsulated carbon nanotube for a Li-ion battery anode by DFT calculations. *J Phys Chem C*. 2010;114:8542–8545.
38. Jiang Z, Klyukin K, Alexandrov V. First-principles study of adsorption-desorption kinetics of aqueous V^{2+}/V^{3+} redox species on graphite in a vanadium redox flow battery. *Phys Chem Chem Phys*. 2017;19:14897–14901.
39. Hassan A, Haile AS, Tzedakis T, Hansen HA, De Silva P. The role of oxygenic groups and sp^3 carbon hybridization in activated graphite electrodes for vanadium redox flow batteries. *ChemSusChem*. 2021;14:3945–3952.
40. Lee JH, Kim R, Kim S, et al. Dendrite-free Zn electrodeposition triggered by interatomic orbital hybridization of Zn and single vacancy carbon defects for aqueous Zn-based flow batteries. *Energy Environ Sci*. 2020;13:2839–2848.
41. Neese F. The ORCA program system. *Wires Comput Mol Sci*. 2012;2:73–78.
42. Neese F, Wennmohs F, Becker U, Riplinger C. The ORCA quantum chemistry program package. *J Chem Phys*. 2020;152:224108.
43. Neese F. Software update: the ORCA program system—version 5.0. *Wires Comput Mol Sci*. 2022;12:e1606.
44. Stephens PJ, Devlin FJ, Chabalowski CF, Frisch MJ. Ab initio calculation of vibrational absorption and circular dichroism spectra using density functional force fields. *J Phys Chem*. 1994;98:11623–11627.
45. Grimme S, Antony J, Ehrlich S, Krieg H. A consistent and accurate ab initio parametrization of density functional dispersion correction (DFT-D) for the 94 elements H-Pu. *J Chem Phys*. 2010;132:154104.
46. Weigend F, Ahlrichs R. Balanced basis sets of split valence, triple zeta valence and quadruple zeta valence quality for H to Rn: design and assessment of accuracy. *Phys Chem Chem Phys*. 2005;7:3297–3305.
47. Mardirossian N, Head-Gordon M. ω B97M-V: a combinatorially optimized, range-separated hybrid, meta-GGA density functional with VV10 nonlocal correlation. *J Chem Phys*. 2016;144:214110.
48. Marenich AV, Cramer CJ, Truhlar DG. Universal solvation model based on solute electron density and on a continuum model of the solvent defined by the bulk dielectric constant and atomic surface tensions. *J Phys Chem B*. 2009;113: 6378–6396.
49. Ásgeirsson V, Birgisson BO, Bjornsson R, et al. Nudged elastic band method for molecular reactions using energy-weighted springs combined with eigenvector following. *J Chem Theor Comput*. 2021;17:4929–4945.
50. Fukui K. The path of chemical reactions-the IRC approach. *Acc Chem Res*. 1981;14: 363–368.
51. Fukui K. Formulation of the reaction coordinate. *J Phys Chem*. 1970;74:4161–4163.
52. Neese F, Wennmohs F, Hansen A, Becker U. Efficient, approximate and parallel Hartree–Fock and hybrid DFT calculations. A 'chain-of-spheres' algorithm for the Hartree–Fock exchange. *Chem Phys*. 2009;356:98–109.
53. Evans DJ, Holian BL. The Nose-Hoover thermostat. *J Chem Phys*. 1985;83: 4069–4074.
54. Bussi G, Donadio D, Parrinello M. Canonical sampling through velocity rescaling. *J Chem Phys*. 2007;126:014101.
55. Lu T, Chen F. Multiwfn: a multifunctional wavefunction analyzer. *J Comput Chem*. 2012;33:580–592.
56. Lu T, Chen F. Quantitative analysis of molecular surface based on improved Marching Tetrahedra algorithm. *J Mol Graph Model*. 2012;38:314–323.
57. Lu T, Chen F. Comparison of computational methods for atomic charges. *Acta Phys Chim Sin*. 2012;28:1–18.
58. Lu T, Chen Q. Interaction region indicator: a simple real space function clearly revealing both chemical bonds and weak interactions. *Chem Methods*. 2021;1: 231–239.
59. Zhang J, Lu T. Efficient evaluation of electrostatic potential with computerized optimized code. *Phys Chem Chem Phys*. 2021;23:20323–20328.
60. Humphrey W, Dalke A, Schulten K. VMD: visual molecular dynamics. *J Mol Graph Model*. 1996;14:33–38.
61. Murray JS, Politzer P. Electrostatic potentials: chemical applications. *Encycl Comput Chem*. 2002;2. https://doi.org/10.1002/0470845015.cca014.
62. Johnson ER, Keinan S, Mori-Sánchez P, Contreras-García J, Cohen AJ, Yang W. Revealing noncovalent interactions. *J Am Chem Soc*. 2010;132:6498–6506.
63. Liu Z, Lu T, Chen Q. Intermolecular interaction characteristics of the all-carboatomic ring, cyclo [18] carbon: focusing on molecular adsorption and stacking. *Carbon*. 2021;171:514–523.
64. Uchikoshi M, Akiyama D, Kimijima KI, Shinoda K. Speciation of chromium aqua and chloro complexes in hydrochloric acid solutions at 298 K. *RSC Adv*. 2022;12: 32722–32736.
65. Zeng Z, Sun Y, Zhang J. The electrochemical reduction mechanism of trivalent chromium in the presence of formic acid. *Electrochem Commun*. 2009;11:331–334.
66. Shin SJ, Kim DH, Bae G, et al. On the importance of the electric double layer structure in aqueous electrocatalysis. *Nat Commun*. 2022;13:174.
67. Weaver MJ, Anson FC. Simple criteria for distinguishing between inner-and outer-sphere electrode reaction mechanisms. *J Am Chem Soc*. 1975;97:4403–4405.
68. Fulton JL, Bylaska EJ, Bogatko S, et al. Near-quantitative agreement of model-free DFT-MD predictions with XAFS observations of the hydration structure of highly charged transition-metal ions. *J Phys Chem Lett*. 2012;3:2588–2593.
69. Ghosh S, Agarwal H, Galib M, et al. Near-quantitative predictions of the first-shell coordination structure of hydrated first-row transition metal ions using K-edge X-ray absorption near-edge spectroscopy. *J Phys Chem Lett*. 2022;13:6323–6330.
70. Bianchini F, Fjellvåg H, Vajeeston P. A first-principle study of $NaMPO_4$ (M= Mn, Fe, Co, Ni) possible novel structures as cathode materials for sodium-ion batteries: structural and electrochemical characterisation. *Mater Chem Phys*. 2018;219: 212–221.
71. Li X, Wang T, Cai Y, et al. Mechanism of cations suppressing proton diffusion kinetics for electrocatalysis. *Angew*. 2023;62:e202218669.
72. Kann ZR, Skinner JL. A scaled-ionic-charge simulation model that reproduces enhanced and suppressed water diffusion in aqueous salt solutions. *J Chem Phys*. 2014;141:104507.

Xiaojun Zhao received his Ph.D. degree from North China Electric Power University (NCEPU) in 2011 and was a visiting scholar at Griffith University and Graz University of Technology. Since 2021, he has been working at the Department of Electrical Engineering of NCEPU as a professor. His major research focuses on key materials of high-performance flow batteries and lithium batteries and energy storage technology applications in new energy power systems.

Hao Li received his Ph.D. degree from the University of Texas at Austin in 2019 and then was a postdoctoral researcher at the Catalysis Theory Center at the Technical University of Denmark. Since 2022, he has been working at the Advanced Institute for Materials Research (WPI-AIMR) of Tohoku University as an associate professor and group leader. His major research focuses on the development of materials theory and the development of computation methods based on artificial intelligence.

Weijie Yang received his Ph.D. degree from North China Electric Power University (NCEPU) in 2019. Since 2022, he has been working at the Department of Energy Power and Mechanical Engineering of NCEPU as an associate professor. He became the director of the Teaching and Research Section of Hydrogen Energy Science and Engineering in 2022. He was selected for 2023 Stanford's List of World's Top 2% Scientists. His major research focuses on DFT and ML for hydrogen storage materials and advanced catalysis.